

Nodal-line plasmons in ZrSiX ($X = \text{S, Se, Te}$) and their temperature dependenceYi Li,^{1,2,*} Maoyuan Wang,^{3,*} Yong Li,^{1,2,*} Siwei Xue,¹ Jiade Li,^{1,2} Zhiyu Tao,^{1,2} Xin Han,^{1,2} Jianhui Zhou,^{4,†}
Youguo Shi,^{1,5} Jiandong Guo,^{1,2,5,‡} and Xuetao Zhu^{1,2,5,§}¹Beijing National Laboratory for Condensed Matter Physics and Institute of Physics, Chinese Academy of Sciences, Beijing 100190, China²School of Physical Sciences, University of Chinese Academy of Sciences, Beijing 100049, China³Department of Physics, Xiamen University, Xiamen 361005, China⁴Anhui Province Key Laboratory of Condensed Matter Physics at Extreme Conditions, High Magnetic Field Laboratory, HFIPS, Chinese Academy of Sciences, Hefei 230031, China⁵Songshan Lake Materials Laboratory, Dongguan, Guangdong 523808, China

(Received 8 January 2023; revised 7 March 2023; accepted 4 April 2023; published 18 April 2023)

Topological nodal-line semimetals gain extensive attention for their peculiar linear band crossings along closed lines in the Brillouin zone leading to various interesting properties. Here, we systematically study the nodal-line plasmons of prototypical nodal-line semimetals ZrSiX ($X = \text{S, Se, Te}$) by high-resolution electron energy loss spectroscopy, and first-principles calculations. In energy range from near- to mid-infrared frequencies, plasmons induced by the intraband correlations (~ 0.8 eV) and the interband correlations (~ 0.3 eV) of surface states related to the nodal-line electrons are universally observed in all the ZrSiX family. The bulk plasmon (~ 0.6 eV) is observed in ZrSiS but is indiscernible in both ZrSiSe and ZrSiTe owing to their stronger screening effect from the surface states and large interlayer distance. Although the plasmons in ZrSiS seem to be temperature independent, the frequencies of the intraband plasmons in ZrSiSe and ZrSiTe show large redshifts ($\sim 10\%$) with temperature increasing from 30 K to room temperature, which can be ascribed to the prominent thermal occupation effect of nodal-line electrons when the Fermi level is close to the nodal line.

DOI: [10.1103/PhysRevB.107.155421](https://doi.org/10.1103/PhysRevB.107.155421)**I. INTRODUCTION**

Topological semimetals, a family of new quantum materials, have triggered much interest for their topological bulk and nontrivial surface states, germane to linear band crossing [1,2]. According to the dimension of the band crossing points in the momentum space, topological semimetals can be classified into Dirac (Weyl) semimetals with discrete Dirac (Weyl) points and nodal-line semimetals (NLSM) with nodal lines or rings. In Dirac (Weyl) semimetals, plasmons, the collective excitations of electrons, are theoretically predicted to exhibit various fascinating properties [3–11] such as anomalous temperature dependence [4], anisotropy due to the Fermi-arc surface states [8], and nonreciprocity induced by the chiral anomaly [11]. Many experiments in Dirac (Weyl) semimetals have observed unconventional plasmons originating from topological electronic states [12–14]. Remarkably, in NLSM, plasmons are also predicted to demonstrate interesting properties such as unique carrier density dependence [15], anisotropy due to the toroidal Fermi surface [16], and gapless spin-wave mode induced by population imbalance [17]. In particular, recent experiment has elucidated the existence

of nodal-line plasmons originating from the correlations of nodal-line states and the relevant surface states in ZrSiS [18].

As a prototype of NLSM, ZrSiX ($X = \text{S, Se, Te}$) hosts topological nodal lines protected by nonsymmorphic symmetry and linearly dispersing bands at the Fermi energy E_F extending over up to 2 eV energy range [19–23]. This class of materials exhibits exceptional properties such as unusual magnetoresistance [24] and ultrahigh mobility of charge carriers [25]. From the perspective of collective excitations, the isostructure and similar band structure in the ZrSiX family [19] implies similar plasmon behavior in ZrSiSe and ZrSiTe to that in ZrSiS. On the other hand, the structure ratio c/a , where a and c are the in-plane and out-of-plane lattice parameters, respectively, increases with the increase of the atomic size of the chalcogen element from S to Se, Te, implying weaker interlayer bonding and more two-dimensional-like (2D-like) characteristics [23]. The different interlayer bonding strength implies the distinct out-of-plane hopping parameters between layers and usually modifies the energy bands of both the bulk states and the relevant surface states, such as the projection of bulk states near the surface and the screening of bulk states from the surface states. Consequently, the tunable interlayer bonding strength in the ZrSiX family can be used to tailor the properties of plasmons therein. However, the influence of the interlayer bonding strength on the properties of plasmons in ZrSiX remains elusive, since the experimental evidences of nodal-line plasmons in ZrSiSe and ZrSiTe are still lacking. Besides, the nodal lines in ZrSiX guarantee the presence of topologically protected drumhead surface states (DSS) or

*These authors contributed equally to this work.

†jhzhou@hmfl.ac.cn

‡jdguo@iphy.ac.cn

§xtzhu@iphy.ac.cn

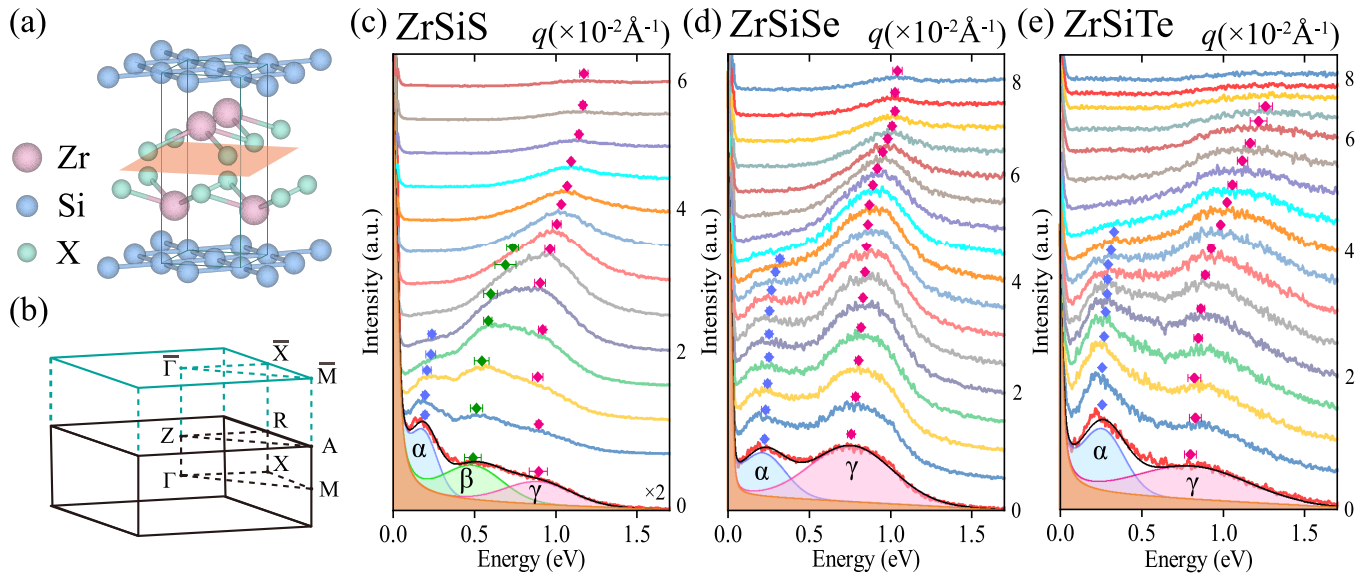


FIG. 1. (a) Crystal structure of ZrSiX ($X = \text{S, Se, Te}$). The orange plane represents the cleavage plane between the X atom layers along the (001) direction. (b) The bulk and surface Brillouin zone of ZrSiX . (c)–(e) Stacks of momentum-dependent EDCs, with the corresponding momentum values on the right, along the $\bar{\Gamma}\bar{M}$ direction of ZrSiS , ZrSiSe , and ZrSiTe , respectively. At the bottom the EDCs at $q = 0$ have been fitted with three or two Gaussian peaks and Drude background (the shaded orange areas). The plasmon peak positions are indicated with error bars from fitting procedure and experimental error. Data along the $\bar{\Gamma}\bar{X}$ direction can be found in the SM [29] without significant difference.

other surface states [26–28], which may give rise to distinct surface plasmon behaviors.

In this paper, several nodal-line plasmons with energies ranging from the near- to mid-infrared frequencies are observed by high-resolution electron energy loss spectroscopy (HREELS) in ZrSiS , ZrSiSe , and ZrSiTe . Combined with angle-resolved photoemission spectroscopy (ARPES) and first-principles calculations, these plasmons are assigned to the intra- or inter-band correlations of bulk nodal lines and their projected surface states. Strikingly, apart from two universally emerged surface plasmons in the isostructural ZrSiX materials, the bulk plasmon clearly observed in ZrSiS seems to disappear at the surfaces in ZrSiSe and ZrSiTe . The different behavior of the bulk plasmon can be ascribed to the stronger screening effect from the surface states in ZrSiSe and ZrSiTe . We also reveal that the surface interband plasmons in ZrSiS , ZrSiSe , and ZrSiTe actually originate from different surface states. Moreover, unlike the temperature-independent behavior in ZrSiS , the surface intraband plasmons in ZrSiSe and ZrSiTe exhibit a large redshift ($\sim 10\%$) in frequencies with increasing temperature. The temperature-dependent behavior is explained by a phenomenological model for the thermal occupation effect of the nodal-line carriers.

II. PLASMONS AND ORIGINS

The class of compounds ZrSiX , where X is a chalcogen atom ($X = \text{S, Se, Te}$), crystallizes in a PbFCl -type structure in the tetragonal $P4/nmm$ (No. 129) space group, containing five-layer square nets with a stacking sequence [Si-Zr-X-X-Zr] [23], as shown in Fig. 1(a). Experimentally, the cleavage occurs between the two adjacent Zr-X layers along the (001) direction, due to the weak Van de Waals bonding. Figure 1(b) shows the bulk and surface Brillouin zones of the tetragonal

structure. According to the calculated electronic structure of ZrSiX [23,28,30], only the linear bands related to the nodal lines are dominant at E_F , and thus the properties of ZrSiX are dominated by the nodal-line states. As the electronic collective excitations in ZrSiX , the surface plasmons are mainly determined by three kinds of surface electronic states: (i) the topologically protected DSS mentioned previously, (ii) the hybrid surface states (HSS), which appear on the upper edge of the projected bulk nodal-line bands onto the surface, and (iii) the floating surface states (FSS), which is the consequence of the breaking of the nonsymmorphic symmetries at the cleaved surface [31].

In this study, single crystalline samples of ZrSiS , ZrSiSe , and ZrSiTe were grown by chemical vapor transport method. All the samples were cleaved under an ultrahigh vacuum of 2.0×10^{-10} mbar to obtain the (001) surface. The surface quality and the crystallography direction were checked by *in situ* low-energy electron diffraction. The electronic structures were characterized at 35 K by *in situ* ARPES using a UV light at 21.2 eV from Scienta VUV5000 helium lamp source. Then the plasmon dispersions were measured by *in situ* HREELS, which is a powerful technique to probe vibrational or electronic excitations through the interaction between the incident electrons and solid surface. In the so-called dipole scattering regime, the incident electrons can be treated similarly as an infrared electromagnetic wave that interacts, at long range, with oscillating dipoles created by the charge density oscillations, i.e., the plasmons. From our HREELS measurements, the plasmon energy, which equals the energy loss of incident electrons, as well as the plasmon momentum determined by the incident and scattering angles, can be simultaneously obtained [32]. Most of the HREELS measurements were performed with an incident beam energy $E_i = 110$ eV and an incident angle of 60° unless specified otherwise. Details about

the sample preparation and characterization were described in the Supplemental Material (SM) [29].

Figures 1(c)–1(e) illustrate the stacks of momentum-dependent energy distributions curves (EDCs), with the corresponding momentum values on the right, along the $\overline{\Gamma\text{M}}$ direction of ZrSiS, ZrSiSe, and ZrSiTe, respectively. From the EDCs, several energy loss peaks are observed clearly between 0.1 eV and 1.5 eV, especially in the small momentum range. Their frequencies and prominent damping characteristics manifest the nature of plasmons. Besides, the EDCs along the $\overline{\Gamma\text{X}}$ direction (see details in the SM [29]) are similar to those along the $\overline{\Gamma\text{M}}$ direction, implying isotropic characteristics of the plasmons. From the model of an ideal nodal ring, the theoretically predicted plasmon dispersions are different along the directions parallel and perpendicular to the nodal-ring plane [16]. This predicted anisotropic plasmon feature from a simple model is not the case here due to the complicated distributions of nodal lines in the three-dimensional (3D) Brillouin zone of ZrSiX [28]. Especially, although the overall band structures of ZrSiX are anisotropic, the most prominent feature is the Dirac cones with similar Fermi velocity in both $\overline{\Gamma\text{X}}$ and $\overline{\Gamma\text{M}}$ directions. And as will be discussed later, the plasmons observed in this work originate from the band correlations related to these Dirac cones around the Fermi level, i.e., the electronic states effectively contributing to the plasmons are actually isotropic. To gain a better understanding, the EDCs were fitted by Gaussian peaks with the Drude background subtracted (see details in the SM [29]). The fitted peak positions are depicted as colored diamonds in the figures. The error bars come from the fitting procedure due to the uncertainty from different background subtractions, and the experimental error estimated by the full width at half maxima (FWHM) of the specular peak (~ 5 meV). From these fittings, the peaks α (~ 0.3 eV), β (~ 0.6 eV), and γ (~ 0.8 eV) can be clearly discerned in ZrSiS, consistent with our previous study [18]. However, in ZrSiSe and ZrSiTe, the peaks α and γ still exist while the peaks β are indiscernible.

All the dispersions of aforementioned plasmons are summarized in Figs. 2(a)–2(c) for ZrSiS, ZrSiSe, and ZrSiTe, respectively. To elucidate the nature of the measured plasmon modes, we carried out an ARPES measurement [Figs. 2(d)–2(f)] to determine the position of the Fermi level, and first-principle calculations for a quantitative understanding of the plasmon dispersions. From a 20-layer slab model, the electronic band structures are obtained and shown in Figs. 2(g)–2(i), with the Fermi level depicted as green dashed lines. The ARPES mapping and the calculated band structures are well consistent, all showing conspicuous linear-dispersing nodal-line states. Furthermore, the plasmons can be revealed as sharp peaks in the electron energy-loss functions [33],

$$L(\mathbf{q}, \omega) = \text{Im} \left[\frac{-1}{\varepsilon^{(\text{RPA})}(\mathbf{q}, \omega)} \right], \quad (1)$$

and the dynamical dielectric functions within the random phase approximation (RPA) are given as [34]

$$\varepsilon^{(\text{RPA})}(\mathbf{q}, \omega) = 1 - v_q \Pi(\mathbf{q}, \omega), \quad (2)$$

where v_q is the 3D Coulomb interaction, and $\Pi(\mathbf{q}, \omega)$ is the density-density correlation function, which can be obtained by the calculated electronic band structure.

Using Eqs. (1) and (2), the layer-dependent dielectric functions as well as the energy-loss functions were acquired (see details in the SM [29]), and several plasmons were obtained and shown as black solid lines in Figs. 2(a)–2(c). Within the RPA method, the calculated plasmon dispersions match well with the experimental results, except for the deviation at large momentum due to the electron-electron correlations beyond RPA. The origin of each plasmon mode can be determined through a comparison between the calculated plasmon dispersions and the experimental results. It turns out that the plasmons α and γ are related to the surface states. The plasmons γ , observed in all the cases of ZrSiS, ZrSiSe, and ZrSiTe, are originated from the intraband correlations of the HSS. For the plasmons α , the origins are slightly different. In ZrSiS, as shown in Fig. 2(g), it comes from the interband correlations between the HSS and the FSS. In ZrSiSe, with the FSS away from the Fermi level [Fig. 2(h)], the interband correlations between the upper bands and lower bands of the HSS instead play a crucial role. In ZrSiTe, the well-known DSS is much more prominent [Fig. 2(i)], and the interband plasmon is mainly due to the interband correlations between the DSS and the HSS. Furthermore, the HREELS measurements with varying incident angles of the electron beam indicate that the grazing incidence can enhance the intensities of the plasmons around ~ 0.8 eV and ~ 0.3 eV (see details in the SM [29]), consolidating their surface nature.

The plasmon β , which is ascribed to the intraband correlations of the bulk nodal-line electrons around the Fermi level [18], only appears in ZrSiS but becomes invisible at the surfaces of ZrSiSe and ZrSiTe. This can be explained by the electronic density of states (DOS) calculated from the bulk and surface electronic states in ZrSiX [as illustrated in Figs. 2(j)–(l)]. It is clear that, around the Fermi level, the difference between the DOS of surface states and bulk states (pink shaded area) increases from ZrSiS to ZrSiSe and ZrSiTe, suggesting the increasing screening effect from the surface states to the bulk states. In ZrSiS, around the Fermi level, the bulk states have similar DOS to the surface states, thus the screening effect is weak and the bulk plasmon β is observed. However, in ZrSiSe and ZrSiTe, probably due to the weaker interlayer bonding caused by the larger lattice parameter c (interlayer spacing) [23], the surface states have higher DOS than the DOS of the projected bulk states near the surface. Hence the bulk plasmons are more effectively screened and become weakened by the surface states and thus are invisible in ZrSiSe and ZrSiTe.

III. TEMPERATURE EFFECTS

Temperature dependence of plasmons could reveal the nature of electronic states in materials. Temperature-dependent HREELS measurements (see details in the SM [29]) of the three materials were performed to investigate the possible thermal effects on the observed nodal-line plasmons, with the results shown in Fig. 3. In ZrSiS all three plasmons show no discernible temperature dependence in energy. In ZrSiSe and ZrSiTe, however, although the α plasmons are almost temperature independent, the γ plasmons exhibit clear energy softening ($\sim 10\%$) with increasing temperature from 35 K to room temperature. For further confirmation, the dispersions of

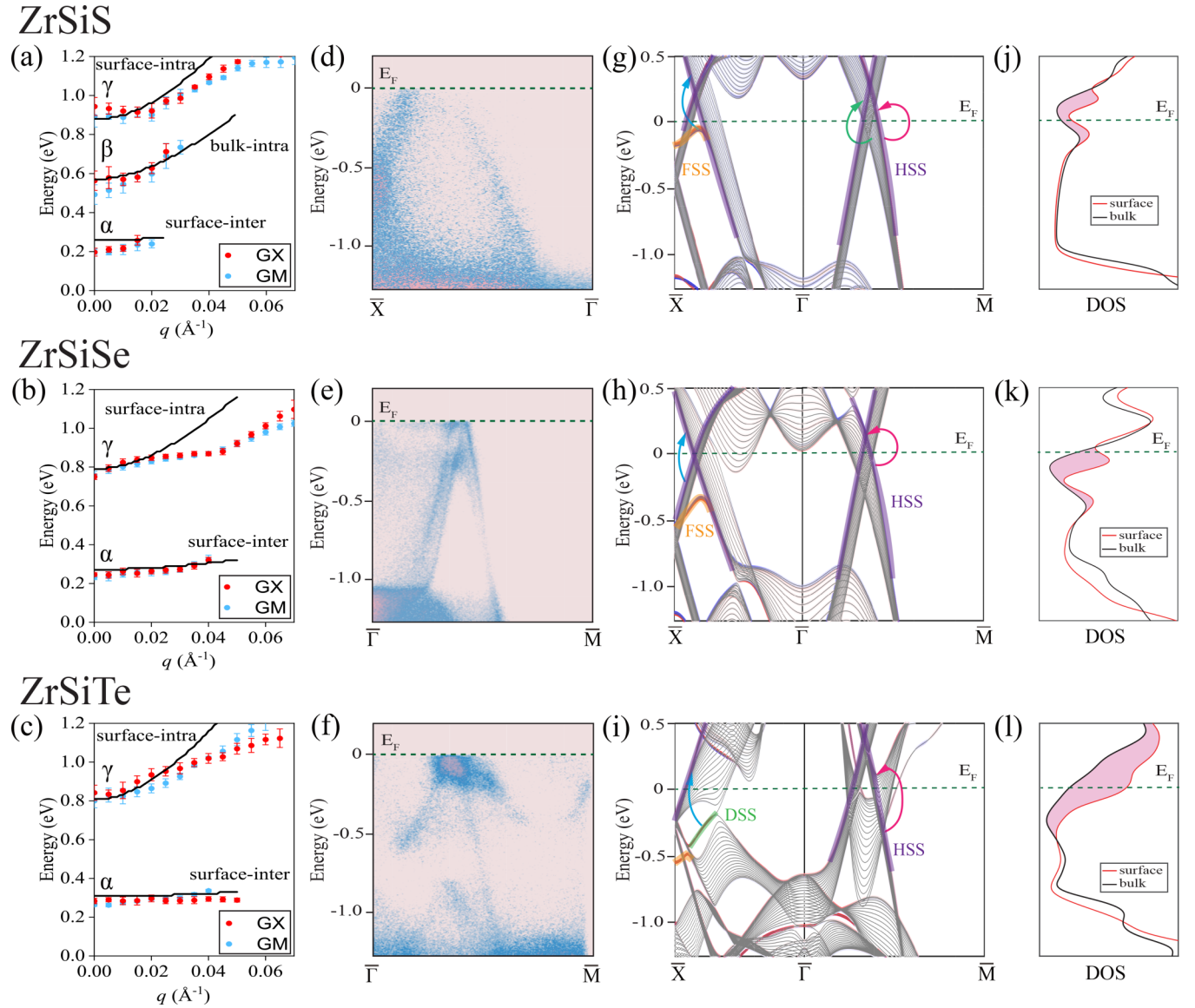


FIG. 2. For ZrSiS, ZrSiSe, ZrSiTe, respectively: (a)–(c) Comparison between the extracted experimental plasmon peaks (red and blue dots) and the calculated loss function peaks (black lines). (d)–(f) ARPES images obtained at 35 K. The green dashed lines represent the Fermi levels. (g)–(i) Calculated electronic dispersions of a 20-layer slab along the $\bar{X} - \bar{\Gamma} - \bar{M}$ path. The gray solid lines are the surface projected bulk bands, while the surface states HSS, FSS, and DSS are indicated by the purple, orange, and green solid lines, respectively. The green dashed line is the Fermi level obtained from ARPES. The blue arrow corresponds to the interband correlations, while the pink and green arrows sketch the intraband correlations. (j)–(l) The calculated DOS for surface states (red line) and bulk states (black line). The difference between the DOS of surface states and bulk states around the Fermi level is emphasized as pink area.

these plasmons at 35 K and room temperature are measured with the results illustrated in Figs. 3(d)–3(f). In ZrSiS the dispersions of all the plasmons at low temperature show no obvious difference from the case at room temperature. In ZrSiSe and ZrSiTe, while the α plasmons show no temperature dependence, the γ plasmons exhibit apparent softening behavior at room temperature in the small momentum range. With the increasing momentum, the temperature effect weakens and the plasmons at 35 K and room temperature merge into the same dispersion.

In order to clarify the nature of the different temperature-dependent behaviors of these plasmons, we analyze the experimental results with a simple phenomenological model.

The thermal variation of the carrier distribution was reported previously, responsible for the substantial temperature effects on plasmons in Dirac systems with relatively low Fermi levels [4,35]. Similarly, we consider the chemical potential μ of a nodal ring first. At $T = 0$, μ equals to the Fermi energy E_F . At finite temperature T , μ is determined by

$$\int_0^{\infty} f(E)N(E)dE = \int_0^{E_F} N(E)dE, \quad (3)$$

where $f(E) = 1/(1 + e^{(E-\mu)/k_B T})$ is the Fermi-Dirac distribution function, k_B is the Boltzmann constant, and $N(E)$ is the DOS. At the low-temperature limit, the analytical

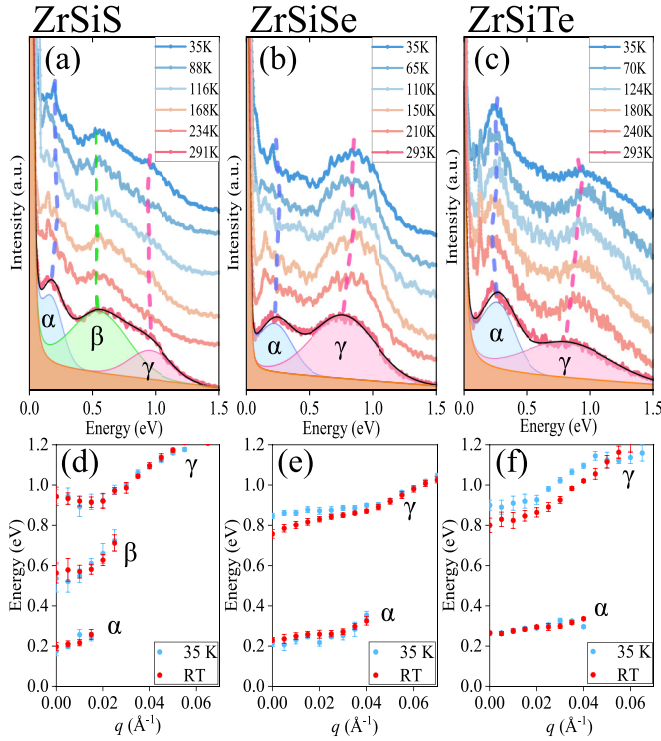


FIG. 3. (a)–(c) Stacks of temperature-dependent EDCs at $q = 0$, along the $\bar{\Gamma}\text{M}$ direction of ZrSiS, ZrSiSe, and ZrSiTe, respectively. At the bottom the EDCs at room temperature have been fitted with three or two Gaussian peaks and Drude background (the shaded orange areas). The dashed lines are guide lines for temperature-dependent peak positions. (d)–(f) Dispersions of plasmons at room temperature (red dots) and 35 K (blue dots) with error bars, along the $\bar{\Gamma}\text{M}$ direction of ZrSiS, ZrSiSe, and ZrSiTe, respectively.

approximation [36] is given as

$$\mu(T) \approx E_F \left[1 - \frac{\pi^2}{6} \frac{N'(E_F)}{N(E_F)} \frac{(k_B T)^2}{E_F} \right], \quad (4)$$

where $N'(E_F)$ is the derivative of $N(E_F)$.

Besides, since a 3D nodal line is equivalent to a collection of continuous 2D Dirac points connecting each other along the third dimension, the 3D nodal line has the same low-energy DOS $N(\varepsilon) \propto \varepsilon$ as a 2D Dirac point (ε is energy relative to the Dirac point at $\varepsilon = 0$). Substituting $N(\varepsilon) \propto \varepsilon$ into Eq. (4) yields

$$\mu/\varepsilon_F = 1 - \frac{\pi^2}{6} \left(\frac{k_B T}{\varepsilon_F} \right)^2, \quad (5)$$

where ε_F represents the energy difference between the Fermi level and the Dirac point.

With increasing temperature, the chemical potential μ shifts down and moves closer to the Dirac point, as shown in Fig. 4(a). And smaller ε_F would lead to a more prominent temperature-induced shift of μ . Thus, when the Fermi level is lower and closer to the Dirac point, the chemical potential goes faster to the Dirac point with increasing temperature. Furthermore, at zero temperature, the plasmon energy at $q = 0$ of a nodal ring is given by [3,16] $\omega_0^{T=0} \propto \varepsilon_F^{1/2}$, and at finite temperature we have $\omega_0 \propto \mu^{1/2}$. Combining it with Eq. (5) we

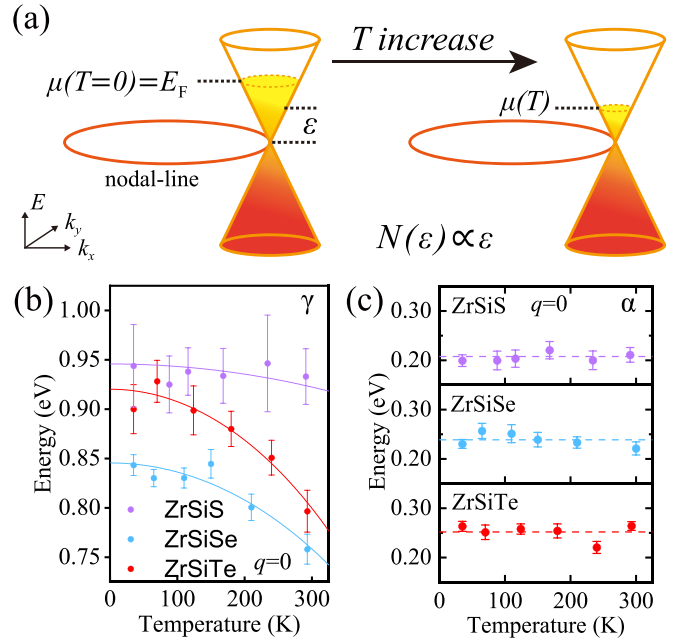


FIG. 4. (a) Schematic of the evolution of chemical potential of an ideal nodal-ring electronic structure with increasing temperature. (b) The experimental temperature dependence of the surface intraband plasmon energy for ZrSiS, ZrSiSe, ZrSiTe (dots with error bars) and fittings (lines) using the thermal occupation effect model. (c) The experimental temperature dependence of the surface interband plasmon energy for ZrSiS, ZrSiSe, ZrSiTe (dots with error bars). The dashed lines are guide lines.

get

$$\omega_0/\omega_0^{T=0} = \left[1 - \frac{\pi^2}{6} \left(\frac{k_B T}{\varepsilon_F} \right)^2 \right]^{1/2}. \quad (6)$$

The temperature dependence of the chemical potential of the nodal-line semimetals results in the plasmon energy softening behavior with increasing temperature (referred to as the thermal occupation effect here for simplicity; see details in the SM [29]). Note that this simplified model is also applied to the case of the hole carriers when the Fermi level is below the nodal ring.

Using Eq. (6), the experimental results of the surface intraband plasmons in ZrSiX, which exhibits obvious temperature dependence, were fitted with the results shown in Fig. 4(b). The reduction in the energy of the surface intraband plasmon with the increasing temperature only depends on the energy difference between the Fermi level and the Dirac point. It is noteworthy that the nodal lines in ZrSiX itself have energy dispersion in the Brillouin zone [37], and thus the simplified model used here only reflects the effective energy difference between Fermi levels and the nodal lines. From the fittings the effective Fermi levels ε_F can be extracted for ZrSiS (≥ 150 meV), ZrSiSe (~ 70 meV), and ZrSiTe (~ 70 meV), consistent with our ARPES measurements in Figs. 2(d)–2(f). In ZrSiS, since its Fermi level is far away from the nodal lines (≥ 150 meV), the thermal occupation effect is weak according to Eq. (6). Therefore, the surface intraband plasmon in ZrSiS shows no discernible temperature dependence. In contrast, the

Fermi level is close to the nodal lines in ZrSiSe and ZrSiTe, which leads to a prominent thermal shift of the chemical potential, resulting in the temperature-dependent behavior of the surface intraband plasmon. Similar temperature dependence of plasmons in several Dirac systems due to thermal occupation effect have been reported [38–40]. Recall that the surface interband plasmons around ~ 0.3 eV in all three systems seem to be temperature independent [shown in Fig. 4(c)]. It is possible that due to the lower energies of these plasmons (~ 0.3 eV), the corresponding energy decreases at room temperature [~ 30 meV if the softening fraction is the same as the intraband plasmons ($\sim 10\%$)] is within the error bars of our HREELS measurement and is hard to be determined. Besides, unlike the intraband plasmons, whose frequency is proportional to the number of coherent electron-hole pairs near the Fermi surface and thus sensitive to the temperature, the number of interband electron-hole pairs instead becomes insensitive to the thermal effect within a moderate temperature region. The quite distinct behavior against the temperature between α and γ also implies the interband nature of α .

Apart from the thermal occupation effect, another possible cause for the observed temperature dependence of the plasmons could be the lattice expanding or shrinking with temperature. Generally, with increasing temperature the lattice of normal metals, such as Pb, Al, and Ag, will expand due to the thermal expansion, and consequently, the carrier concentration and the plasmon energy will reduce by a ratio of about 1% [41,42]. The temperature-dependent x-ray diffraction (XRD) measurement of ZrSiSe reports a slightly temperature-induced variation of lattice parameters around 0.4% [30], which is hardly responsible for the plasmon softening behavior observed here in ZrSiSe and ZrSiTe around 10%.

It is worth noting that due to the thermal occupation effect, the chemical potential in Dirac materials will shift to the Dirac point when the temperature is high enough, and then the temperature dependence of the plasmon energy will be dominated by the thermally excited carriers for intrinsic systems. This transition of the plasmonic temperature-dependent behavior has been theoretically predicted [4] and experimentally observed [35].

In Dirac semimetals and Weyl semimetals, the thermal occupation effect on plasmons should be more prominent than that in nodal-line semimetals, because the DOS of

3D Dirac/Weyl semimetals [$N(\epsilon) \propto \epsilon^2$] generates significant temperature-dependent change in the plasmon energy ($\omega_0 \propto \mu$) [6]. Besides, it is suggested that the significant temperature effect on plasmons induced by the thermal occupation effect is a hallmark of semimetallic materials with the Fermi level close to the minimum position in the DOS [43]. In normal metals, which have large DOS near the Fermi level, the temperature dependence of the plasmon energy is usually negligible.

IV. CONCLUSION

In summary, we performed systematic investigations on the nodal-line plasmons and their temperature dependence in the nodal-line semimetal family ZrSiX ($X = \text{S, Se, Te}$). Surface plasmons associated with the interband or intraband correlations of distinct surface states were observed in all three materials. Meanwhile, the bulk plasmon observed in ZrSiS is undetectable by HREELS in ZrSiSe and ZrSiTe due to the stronger screening effect from surface states therein, qualifying ZrSiSe and ZrSiTe as suitable NLSM platforms to study the plasmonic properties due to the topologically protected surface states. Moreover, in ZrSiSe and ZrSiTe, since Fermi levels are close to the nodal lines, resulting in the thermal occupation effect to the nodal-line electrons, the surface intraband plasmons show large redshifts ($\sim 10\%$) with increasing temperature. These unique properties of the nodal-line plasmons in the ZrSiX family facilitate their plasmonics or optics device applications in the near- to mid-infrared frequency range [44].

ACKNOWLEDGMENTS

This work was supported by the National Key R&D Program of China (Grants No. 2021YFA1400200 and No. 2022YFA1403000), the National Natural Science Foundation of China (Grants No. 12274446, No. 12174394, No. 11874404, and No. U2032204), the Strategic Priority Research Program of the Chinese Academy of Sciences (Grant No. XDB33000000), and the Informatization Plan of Chinese Academy of Sciences (CAS-WX2021SF-0102). J.Z. was supported by the High Magnetic Field Laboratory of Anhui Province.

-
- [1] H. Gao, J. W. Venderbos, Y. Kim, and A. M. Rappe, Topological semimetals from first principles, *Annu. Rev. Mater. Res.* **49**, 153 (2019).
 - [2] H. Weng, X. Dai, and Z. Fang, Topological semimetals predicted from first-principles calculations, *J. Phys.: Condens. Matter* **28**, 303001 (2016).
 - [3] S. Das Sarma and E. H. Hwang, Collective Modes of the Massless Dirac Plasma, *Phys. Rev. Lett.* **102**, 206412 (2009).
 - [4] J. Hofmann and S. Das Sarma, Plasmon signature in Dirac-Weyl liquids, *Phys. Rev. B* **91**, 241108(R) (2015).
 - [5] M. Lv and S.-C. Zhang, Dielectric function, Friedel oscillation and plasmons in Weyl semimetals, *Int. J. Mod. Phys. B* **27**, 1350177 (2013).
 - [6] J. Zhou, H.-R. Chang, and D. Xiao, Plasmon mode as a detection of the chiral anomaly in Weyl semimetals, *Phys. Rev. B* **91**, 035114 (2015).
 - [7] D. E. Kharzeev, R. D. Pisarski, and H.-U. Yee, Universality of Plasmon Excitations in Dirac Semimetals, *Phys. Rev. Lett.* **115**, 236402 (2015).
 - [8] J. C. W. Song and M. S. Rudner, Fermi arc plasmons in Weyl semimetals, *Phys. Rev. B* **96**, 205443 (2017).
 - [9] K. Sadhukhan, A. Politano, and A. Agarwal, Novel Undamped Gapless Plasmon Mode in a Tilted Type-II Dirac Semimetal, *Phys. Rev. Lett.* **124**, 046803 (2020).
 - [10] J. Wang, X. Sui, S. Gao, W. Duan, F. Liu, and B. Huang, Anomalous Dirac Plasmons in 1D Topological Electrides, *Phys. Rev. Lett.* **123**, 206402 (2019).

- [11] J. Hofmann and S. Das Sarma, Surface plasmon polaritons in topological Weyl semimetals, *Phys. Rev. B* **93**, 241402(R) (2016).
- [12] A. Politano, G. Chiarello, B. Ghosh, K. Sadhukhan, C.-N. Kuo, C. S. Lue, V. Pellegrini, and A. Agarwal, 3D Dirac Plasmons in the Type-II Dirac Semimetal PtTe₂, *Phys. Rev. Lett.* **121**, 086804 (2018).
- [13] X. Jia, M. Wang, D. Yan, S. Xue, S. Zhang, J. Zhou, Y. Shi, X. Zhu, Y. Yao, and J. Guo, Topologically nontrivial interband plasmons in type-II Weyl semimetal MoTe₂, *New J. Phys.* **22**, 103032 (2020).
- [14] C. Wang, Y. Sun, S. Huang, Q. Xing, G. Zhang, C. Song, F. Wang, Y. Xie, Y. Lei, Z. Sun, and H. Yan, Tunable Plasmons in Large-Area WTe₂ Thin Films, *Phys. Rev. Appl.* **15**, 014010 (2021).
- [15] Z. Yan, P.-W. Huang, and Z. Wang, Collective modes in nodal line semimetals, *Phys. Rev. B* **93**, 085138 (2016).
- [16] J.-W. Rhim and Y. B. Kim, Anisotropic density fluctuations, plasmons, and Friedel oscillations in nodal line semimetal, *New J. Phys.* **18**, 043010 (2016).
- [17] S. K. Firoz Islam and A. A. Zyuzin, Collective modes in an imbalanced nodal-line semimetal, *Phys. Rev. B* **104**, 245301 (2021).
- [18] S. Xue, M. Wang, Y. Li, S. Zhang, X. Jia, J. Zhou, Y. Shi, X. Zhu, Y. Yao, and J. Guo, Observation of Nodal-Line Plasmons in ZrSiS, *Phys. Rev. Lett.* **127**, 186802 (2021).
- [19] B. Salmankurt and S. Duman, First-principles study of structural, mechanical, lattice dynamical and thermal properties of nodal-line semimetals ZrXY (X = Si, Ge; Y = S, Se), *Philos. Mag.* **97**, 175 (2017).
- [20] C. Li, C. M. Wang, B. Wan, X. Wan, H.-Z. Lu, and X. C. Xie, Rules for Phase Shifts of Quantum Oscillations in Topological Nodal-Line Semimetals, *Phys. Rev. Lett.* **120**, 146602 (2018).
- [21] J. Hu, Z. Tang, J. Liu, X. Liu, Y. Zhu, D. Graf, K. Myhro, S. Tran, C. N. Lau, J. Wei, and Z. Mao, Evidence of Topological Nodal-Line Fermions in ZrSiSe and ZrSiTe, *Phys. Rev. Lett.* **117**, 016602 (2016).
- [22] S. Pezzini, M. Van Delft, L. Schoop, B. Lotsch, A. Carrington, M. Katsnelson, N. E. Hussey, and S. Wiedmann, Unconventional mass enhancement around the Dirac nodal loop in ZrSiS, *Nat. Phys.* **14**, 178 (2018).
- [23] J. Ebad-Allah, J. F. Afonso, M. Krottenmüller, J. Hu, Y. L. Zhu, Z. Q. Mao, J. Kuneš, and C. A. Kuntscher, Chemical pressure effect on the optical conductivity of the nodal-line semimetals ZrSiY (Y = S, Se, Te) and ZrGeY (Y = S, Te), *Phys. Rev. B* **99**, 125154 (2019).
- [24] R. Singha, A. K. Pariari, B. Satpati, and P. Mandal, Large non-saturating magnetoresistance and signature of nondegenerate Dirac nodes in ZrSiS, *Proc. Natl. Acad. Sci.* **114**, 2468 (2017).
- [25] R. Sankar, G. Peramaiyan, I. P. Muthuselvam, C. J. Butler, K. Dimitri, M. Neupane, G. N. Rao, M.-T. Lin, and F. Chou, Crystal growth of Dirac semimetal ZrSiS with high magnetoresistance and mobility, *Sci. Rep.* **7**, 40603 (2017).
- [26] C. Fang, Y. Chen, H.-Y. Kee, and L. Fu, Topological nodal line semimetals with and without spin-orbital coupling, *Phys. Rev. B* **92**, 081201(R) (2015).
- [27] R. Yu, Z. Fang, X. Dai, and H. Weng, Topological nodal line semimetals predicted from first-principles calculations, *Front. Phys.* **12**, 127202 (2017).
- [28] L. Muechler, A. Topp, R. Queiroz, M. Krivenkov, A. Varykhalov, J. Cano, C. R. Ast, and L. M. Schoop, Modular Arithmetic with Nodal Lines: Drumhead Surface States in ZrSiTe, *Phys. Rev. X* **10**, 011026 (2020).
- [29] See Supplemental Material at <http://link.aps.org/supplemental/10.1103/PhysRevB.107.155421> for details about sample synthesis and characterization, experimental methods and supplementary data, calculation details, and model of the thermal occupation effect, which includes Refs. [26,28,30–32,45–48].
- [30] F. C. Chen, Y. Fei, S. J. Li, Q. Wang, X. Luo, J. Yan, W. J. Lu, P. Tong, W. H. Song, X. B. Zhu, L. Zhang, H. B. Zhou, F. W. Zheng, P. Zhang, A. L. Lichtenstein, M. I. Katsnelson, Y. Yin, N. Hao, and Y. P. Sun, Temperature-Induced Lifshitz Transition and Possible Excitonic Instability in ZrSiSe, *Phys. Rev. Lett.* **124**, 236601 (2020).
- [31] A. Topp, R. Queiroz, A. Grüneis, L. Muechler, A. W. Rost, A. Varykhalov, D. Marchenko, M. Krivenkov, F. Rodolakis, J. L. McChesney, B. V. Lotsch, L. M. Schoop, and C. R. Ast, Surface Floating 2D Bands in Layered Nonsymmorphic Semimetals: ZrSiS and Related Compounds, *Phys. Rev. X* **7**, 041073 (2017).
- [32] X. Zhu, Y. Cao, S. Zhang, X. Jia, Q. Guo, F. Yang, L. Zhu, J. Zhang, E. Plummer, and J. Guo, High resolution electron energy loss spectroscopy with two-dimensional energy and momentum mapping, *Rev. Sci. Instrum.* **86**, 083902 (2015).
- [33] H. Ibach and D. L. Mills, *Electron Energy Loss Spectroscopy and Surface Vibrations* (Academic Press, Cambridge, 1982).
- [34] G. Giuliani and G. Vignale, *Quantum Theory of the Electron Liquid* (Cambridge University Press, Cambridge, 2005).
- [35] A. B. Sushkov, J. B. Hofmann, G. S. Jenkins, J. Ishikawa, S. Nakatsuji, S. Das Sarma, and H. D. Drew, Optical evidence for a Weyl semimetal state in pyrochlore Eu₂Ir₂O₇, *Phys. Rev. B* **92**, 241108(R) (2015).
- [36] N. W. Ashcroft and N. D. Mermin, *Solid State Physics* (Cengage Learning, Boston, 2022).
- [37] M. M. Hosen, K. Dimitri, I. Belopolski, P. Maldonado, R. Sankar, N. Dhakal, G. Dhakal, T. Cole, P. M. Oppeneer, D. Kaczorowski, F. Chou, M. Z. Hasan, T. Durakiewicz, and M. Neupane, Tunability of the topological nodal-line semimetal phase in ZrSiX-type materials (X = S, Se, Te), *Phys. Rev. B* **95**, 161101(R) (2017).
- [38] T. Vazifeshenas, T. Amlaki, M. Farmanbar, and F. Parhizgar, Temperature effect on plasmon dispersions in double-layer graphene systems, *Phys. Lett. A* **374**, 4899 (2010).
- [39] G. S. Jenkins, C. Lane, B. Barbiellini, A. B. Sushkov, R. L. Carey, F. Liu, J. W. Krizan, S. K. Kushwaha, Q. Gibson, T.-R. Chang, H.-T. Jeng, H. Lin, R. J. Cava, A. Bansil, and H. D. Drew, Three-dimensional Dirac cone carrier dynamics in Na₃Bi and Cd₃As₂, *Phys. Rev. B* **94**, 085121 (2016).
- [40] R. Y. Chen, S. J. Zhang, J. A. Schneeloch, C. Zhang, Q. Li, G. D. Gu, and N. L. Wang, Optical spectroscopy study of the three-dimensional Dirac semimetal ZrTe₅, *Phys. Rev. B* **92**, 075107 (2015).
- [41] A. Imbusch and H. Niedrig, Temperature effect on energy loss spectrum of fast electrons in aluminium and lead foils between 3 K and 295 K, *Phys. Lett. A* **32**, 375 (1970).
- [42] M. Rocca, F. Moresco, and U. Valbusa, Temperature dependence of surface plasmons on Ag(001), *Phys. Rev. B* **45**, 1399 (1992).

- [43] E. T. Jensen, R. E. Palmer, W. Allison, and J. F. Annett, Temperature-Dependent Plasmon Frequency and Linewidth in a Semimetal, *Phys. Rev. Lett.* **66**, 492 (1991).
- [44] T. Stauber, Plasmonics in Dirac systems: from graphene to topological insulators, *J. Phys.: Condens. Matter* **26**, 123201 (2014).
- [45] G. Gatti, A. Crepaldi, M. Puppini, N. Tancogne-Dejean, L. Xian, U. De Giovannini, S. Roth, S. Polishchuk, P. Bugnon, A. Magrez *et al.*, Light-Induced Renormalization of the Dirac Quasiparticles in the Nodal-Line Semimetal ZrSiSe, *Phys. Rev. Lett.* **125**, 076401 (2020).
- [46] A. Ritz and H. Lüth, Experimental Evidence for Surface Quenching of the Surface Plasmon on InSb(110), *Phys. Rev. Lett.* **52**, 1242 (1984).
- [47] A. Politano, V. M. Silkin, I. A. Nechaev, M. S. Vitiello, L. Viti, Z. S. Aliev, M. B. Babanly, G. Chiarello, P. M. Echenique, and E. V. Chulkov, Interplay of Surface and Dirac Plasmons in Topological Insulators: The Case of Bi₂Se₃, *Phys. Rev. Lett.* **115**, 216802 (2015).
- [48] T. Rauch, T. Olsen, D. Vanderbilt, and I. Souza, Geometric and nongeometric contributions to the surface anomalous Hall conductivity, *Phys. Rev. B* **98**, 115108 (2018).